Available online at www.sciencedirect.com

Journal of the European Ceramic Society 28 (2008) 2433–2440

www.elsevier.com/locate/jeurceramsoc

Laser processed protonic ceramics

F.W. Dynys [a,*], M.H. Berger [b], A. Sayir [c]

[a] *NASA-GRC, 21000 Brookpark Road, Cleveland, OH 44135, USA*
[b] *Ecole des Mines de Paris, BP 87, 91003 Evry Cedex, France*
[c] *NASA-GRC/CWRU, 21000 Brookpark Road, Cleveland, OH 44135, USA*

Abstract

High temperature protonic conductors of $SrCe_{0.9}Y_{0.1}O_{3-\delta}$, $Sr_3Ca_{1+x}Nb_{2-x}O_{9-\delta}$ and $BaCe_{0.85}Y_{0.15}O_{3-\delta}$ were fabricated by laser processing. Laser float zone method and pulse laser deposition were used to fabricate dense high temperature protonic ceramic rods and films. Melt growth processing by laser float zone produced textured microstructures with cellular characteristics. Directional solidified $SrCe_{0.9}Y_{0.1}O_{3-\delta}$ contained an aluminium rich inter-granular phase, whereas $Sr_3Ca_{1+x}Nb_{2-x}O_{9-\delta}$ exhibits a cellular microstructure with a decreasing Ca/Nb ratio from the cell center to the cell boundary. A low Ca/Nb ratio is detrimental to proton transport. Nano-domains caused by oxygen cage tilting were observed in both compositions. $Sr_3Ca_{1+x}Nb_{2-x}O_{9-\delta}$ also exhibits stoichiometric domains with an ordered distribution of Nb^{5+} and Ca^{2+} cations. These domains were surrounded by non-stoichiometric domains containing a random cation distribution, which preserves the global stoichiometry and charge neutrality. Electrical impedance spectroscopy revealed similar protonic transport to published data for sintered compositions.

Crystalline $BaCe_{0.9}Y_{0.1}O_{3-\delta}$ films were fabricated on porous substrates at deposition temperatures ranging from 400 to 950 °C. Crystalline films 1–10 μm thick were deposited by excimer laser on porous Al_2O_3 and $BaZrO_3$ substrates. Single-phase $BaCe_{0.85}Y_{0.15}O_{3-\delta}$ films with a columnar growth morphology are observed with preferred crystal growth along the [1 0 0] or [0 0 1] direction. The film electrical conductivity was measured perpendicular to the film growth direction. Impedance measurements show the importance of matching crystal symmetry between substrate and film. High protonic conducting films were achieved by deposition on $BaZrO_3$.

Keywords: Laser; Protonic; Ceramics; Films; Directional solidification

1. Introduction

The perovskite structure, ABX_3, is one of the most versatile crystal structure known in nature. A large class of compounds exists due to numerous crystallographic variations. The structure can accommodate distortions of the ideal cubic structure which provides the capability to incorporate cations of different sizes, tolerate vacancy formation and tolerate atomic-scale intergrowths with other structural motifs. The distorted crystal structure occurs by four mechanisms: (1) distortion of the BX_6 octahedra, (2) displacement of the B-site cation within the octahedron, (3) displacement of the A-site cation and (4) rotations of the octahedra relative to one another. These crystal distortions give rise to unique materials with dielectric, magnetic, electrical, optical, and catalytic properties for technological applications.

High temperature protonic conduction (HTPC) in perovskite based ceramics, $BaCeO_3$ and $SrCeO_3$, was discovered by Iwahar et al.[1] HTPC materials have potential applications as membranes for fuel cells, hydrogen separation and hydrogen generation. To activate proton conduction, a trivalent cation is partially substituted on the B site to create negatively charged defects compensated by oxygen-ion vacancies. Protonic transport has been investigated in numerous ABO_3 type compositions: $A(B'_xB''_{1-x})O_{3-\delta}$, $(A'_xA''_{1-x})BO_{3-\delta}$, $(A'_xA''_{1-x})(B'_xB''_{1-x})O_{3-\delta}$, $A_2(B'_xB''_{1-x})O_{6-\delta}$ and $A_3(B'_{2+x}B''_{2-x})O_{9-\delta}$ These materials are highly selective for hydrogen permeation and exhibit dominant proton transport at temperatures up to 800 °C.[2,3] Combining high protonic conductivity with thermodynamic stability is an essential requirement for HTPC materials for electrochemical applications.

New processes and materials architectures are sought in membrane technology to improve separation efficiencies, transport rates, and membrane life while lowering overall cost of hydrogen generation. Laser processing and laser ablation are mature techniques that are used in material fabrication.[4,5] Laser ablation has the ability to fabricate complex thin film compositions with a nano-crystalline microstructure.[6] Reduction of

---

* Corresponding author.
E-mail address: Frederick.W.Dynys@nasa.gov (F.W. Dynys).

0955-2219/$ – see front matter. Published by Elsevier Ltd.
doi:10.1016/j.jeurceramsoc.2008.03.038

the membrane thickness is desirable to increase the transport rate. Solidified materials via laser processing produce novel microstructures that exhibit excellent mechanical behavior and thermal stability up to temperatures near the melting point. This work demonstrates the feasibility of fabricating HTPC materials by solidification and thin film deposition. Laser float zone (LFZ) method and pulse laser deposition (PLD) were used to fabricate dense HTCP materials. The goal is to improve protonic transport beyond what has been reported for sintered HTCP materials.

2. Experimental

Sintered feed rods of $Sr_3Ca_{2.18}Nb_{1.82}O_{9-\delta}$ and $SrCe_{0.9}Y_{0.1}O_{3-\delta}$ were produced for directional solidification. $Sr_3Ca_{2.18}Nb_{1.82}O_{9-\delta}$ and $SrCe_{0.9}Y_{0.1}O_{3-\delta}$ powders were synthesized using high purity $SrCO_3$ (99.99%), CaO (99.95%), Nb_2O_5 (99.9%) and Y_2O_3 (99.9%) powders obtained from Alpha Aesar. The powders were mixed to the desired stoichometry and ball milled. $Sr_3Ca_{2.18}Nb_{1.82}O_{9-\delta}$ and $SrCe_{0.9}Y_{0.1}O_{3-\delta}$ powders were derived by calcining at 800 and 1000 °C in air for 6 and 10 h, respectively. The calcined powders were cold isostatically pressed into cylindrical rods and sintered in air at 1500 °C for 10 h.

A coherent 2.2 kW CO_2 laser ($\lambda = 10.6\,\mu m$) was used for the LFZ process. The laser beam was split into two beams, 180° apart from each other. Each beam was then focused with ZnSe lenses onto the source rod to create a molten zone. HTCP melting required 800–1100 W of power. Absolute temperature was not measured because the emissivities of the molten Sr–Ce–Y–O and Sr–Ca–Nb–O systems are unknown. A high-density polycrystalline Al_2O_3 seed was brought in contact with the melt to start solidification. The molten zone was maintained by surface tension between seed and sintered rod. The sintered rod was moved vertically at 50 mm/h through the beam incidence area. All solidifications were conducted in air. Fig. 1 shows a directionally solidified rod of $Sr_3Ca_{2.18}Nb_{1.82}O_{9-\delta}$. LFZ produces very high thermal gradients within the sample, which are responsible for some of the novel microstructural features attain.

High-density $BaCe_{0.85}Y_{0.15}O_{3-\delta}$ targets for PLD were fabricated from powders synthesized by solid-state reaction. Targets were sintered at 1650 °C. A previous paper describes the powder synthesis and sintering in more detail.[7] $BaCe_{0.85}Y_{0.15}O_{3-\delta}$ films were grown in a stainless steel high vacuum chamber evacuated to a base pressure of 1×10^{-6} Torr using a turbo molecular pump. A 248-nm KrF excimer laser was used to grow $BaCe_{0.85}Y_{0.15}O_{3-\delta}$ films. The laser conditions for thin film fabrication were a pulse rate of 5 Hz and pulse density ranging from 1.4 to 3 J/cm^2. The target was rotated around its axis to ensure uniform ablation.The angle between target and laser beam was 45°; the target surface was parallel to the substrate surface. Target to substrate distance was kept at 101 mm to obtain sufficient interaction between the plasma plume and the process gas. Substrates were attached to a resistance heater; temperature was monitored by a thermocouple attached to the inner wall of the heater block. Substrate temperature was varied from 400 to 950 °C. Closed loop pressure control was used to maintain a chamber pressure of 20–200 mTorr using O_2 as the process gas. Film growth rate was approximately 0.05 nm/pulse. The as-grown films were cooled to room temperature at a rate of 5 °C/min at O_2 pressures of 20–200 mTorr. No mechanical failures of the $BaCe_{0.85}Y_{0.15}O_{3-\delta}$ film were observed at this cooling rate.

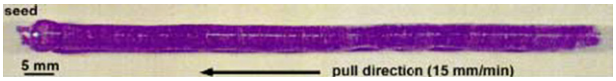

Fig. 1. Directionally solidified $Sr_3Ce_{0.9}Y_{0.1}O_{3-\delta}$ produced using laser heated float zone technique.

Porous Al_2O_3 and $BaZrO_3$ substrates were used for thin film deposition. Al_2O_3 substrates were prepared by pressing Biakowski A-10 powder into discs and sintering the disc at 1100 °C for 1 h to give it sufficient handling strength. $BaZrO_3$ powder obtained from Alpha Aesar was pressed and sintered at 1400 °C to obtain a porous substrate.

The microstructures of the laser processed HTPC materials were studied down to the nano-scale level using scanning electron microscopy (SEM, Zeiss Gemini DSM 982), conventional and high-resolution transmission electron microscopy (TEM, Tecnai 20F ST). Chemical mapping and profiles were determined by wavelength dispersive X-ray analysis (WDX,Cameca SX 50) and analytical scanning transmission electron microscopy (STEM Tecnai 20F ST+EDAX).

X-ray diffraction (XRD) was used to characterize the crystalline nature of synthesized powders and samples. The X-ray diffractometer was equipped with a Cu Kα source with a wavelength of 0.1540 nm. The operating conditions were 45 kV and 40 mA. Scans were conducted at 3°/min with a sampling interval of 0.02°.

Electrical behavior of the materials was studied by high temperature electrochemical impedance spectroscopy (EIS, HP4192/Solartron 1260/1296) from 1 Hz to 13 MHz at temperatures up to 950 °C. Samples were sliced into disks. Platinum or silver electrodes were applied for EIS measurements. Platinum electrodes required a thermal treatment at 1100 °C for 2 h in air. Samples were allowed to equilibrate with temperature and gas environment for 0.5 h or more after stabilization of the temperature. A gas environment of laboratory air (undefined P_{H_2O}) or N_2/H_2 mixture was used for measurements. No special proton loading treatment was performed prior to sample testing. An in-plane electrical configuration was used for thin film EIS measurements as shown in Fig. 2.

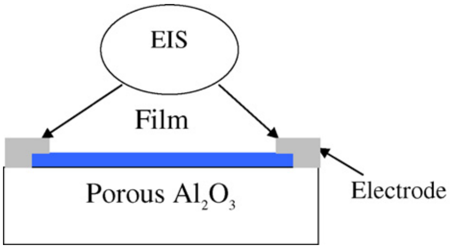

Fig. 2. Sample configuration for electrical impedance spectroscopy.

3. Results and discussion

3.1. Microstructure characterization of directional solidified ceramics

The microstructures of polished longitudinal and cross-sections of $SrCe_{1-x}Y_xO_{3-\delta}$ and $Sr_3Ca_{1+x}Nb_{2-x}O_{9-\delta}$ were examined by SEM. Directional solidification produced textured grains of 10–30 μm in width and several hundred microns in length for both compositions, as shown in Fig. 3. Pore free and unique microstructures were obtained; these microstructures are not achievable by conventional solid-state sintering.

Second phases were observed in $SrCe_{1-x}Y_xO_{3-\delta}$ sample along grain boundaries and triple points. Chemical analysis using WDX revealed that the second phase was enriched in aluminium. The source of Al_2O_3 contamination occurred during sintering as the $SrCe_{1-x}Y_xO_{3-\delta}$ source rods reacted with the Al_2O_3 setter. During melt growth, the perovskite solidified first into elongated grains, rejecting the aluminium rich liquid between the grains, which solidified at a lower temperature. No significant variation of the cationic ratio across the grains could be detected by WDX. Mapping of hydrogen was achieved by forward ^1H scattering with coincidence detection using a nuclear microprobe method.[8] The intergranular aluminium rich second phases were enriched in protons compared to the $SrCe_{0.9}Y_{0.1}O_{3-\delta}$ grains.

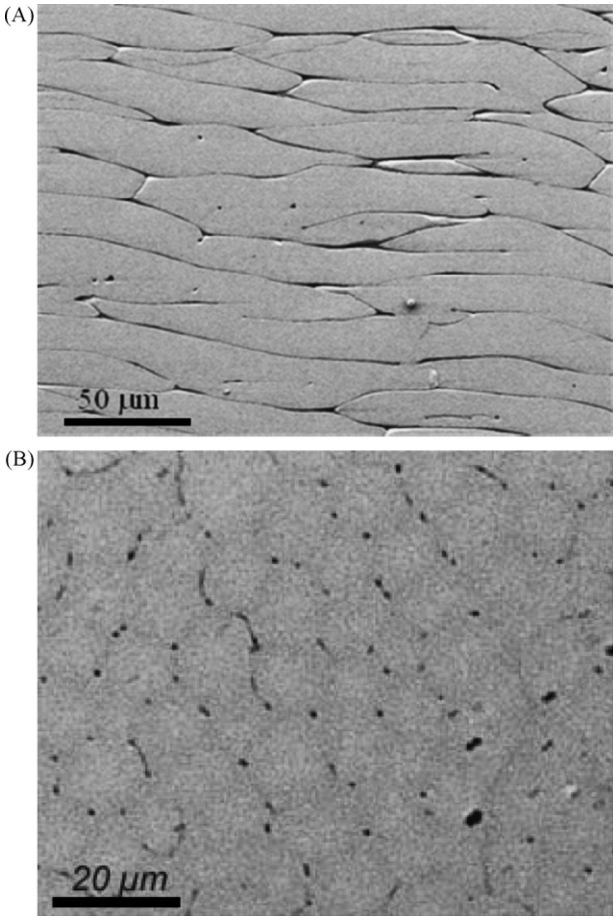

Fig. 3. SEM micrographs of melt grown HTPC: (A) longitudinal section of $SrCe_{0.9}Y_{0.1}O_{3-\delta}$ and (B) transverse section of $Sr_3Nb_{1.82}Ca_{1.18}O_{9-\delta}$.

Aluminium contamination was avoided for $Sr_3Ca_{1+x}Nb_{2-x}O_{9-\delta}$ by using a sacrificial powder layer between the sample and Al_2O_3 setter. A cellular microstructure was observed for $Sr_3Ca_{1+x}Nb_{2-x}O_{9-\delta}$. Inside each $Sr_3Ca_{1+x}Nb_{2-x}O_{9-\delta}$ cell, WDX chemical mapping revealed a chemical gradient. The core or central region of the cells was enriched in calcium and strontium, whereas the outer cell regions were enriched in oxygen and niobium. The calcium content was lower than expected (6–6.25 at% instead of 8 at% for $x = 0.18$). The most probable cause was an error in raw material addition. CaO is reactive with environmental carbon dioxide, causing an overestimation of the CaO mass when the source powders were weighed. The Sr/(Nb + Ca) ratio was higher than 1, (1.13 in the cell cores) revealing some substitution of Sr^{2+} on the *B* sites. Based on the Nb mean concentration of 12.8 at%, a mean substitution level of 0.10 was estimated, with variations from 0.07 in the shell to 0.12 in the core. Intergranular strontium rich second phases were observed at triple junctions and to a minor extent between cells.

3.2. TEM characterization of directional solidified ceramics

Cross sections of $SrCe_{1-x}Y_xO_{3-\delta}$ and $Sr_3Ca_{1+x}Nb_{2-x}O_{9-\delta}$ were ion milled and examined by TEM. Growth axis of the solidified samples corresponded to the ⟨100⟩ direction of a pseudo cubic perovskite cell. The observed grain boundaries were low angle tilt boundaries (less than 10°). Loops attributed to oxygen vacancy grouping were observed in both compositions as shown Fig. 4a. The interior of the cells exhibited domain structures. Domains in $SrCe_{1-x}Y_xO_{3-\delta}$ are separated by planar interfaces as shown in Fig. 4b. Elongated domains with irregular contours are observed for $Sr_3Ca_{1+x}Nb_{2-x}O_{9-\delta}$, as shown in Fig. 4c. Selected area diffraction (SAD) patterns of the cells were recorded in ⟨1 0 0⟩ and ⟨1 1 0⟩ zone axes. The comparison of these SAD patterns with those of a pseudo cubic perovskite structure reveals extra reflections at $(\pm h/2\ k\ l)$, $(\pm h/2 \pm k/2\ l)$ and $(\pm h/2 \pm k/2 \pm l/2)$ for both $SrCe_{1-x}Y_xO_{3-\delta}$ and $Sr_3Ca_{1+x}Nb_{2-x}O_{9-\delta}$. These extra reflections are typical of perovskites with tolerance factor, $t = (R_A + R_O)/\sqrt{2}(R_B + R_O)$, lower than 0.985.[9] For such perovskites, the ionic radii of the *A* site species are too small to occupy the available volume fully. Oxygen octahedra rotate in order to reduce the size of the cuboctahedral interstices of the oxygen sublattice.[10] The results indicate in-phase and anti-phase tilting of the oxygen octahedral as revealed by the extra reflections at $(\pm h/2 \pm k/2\ l)$ and $(\pm h/2 \pm k/2 \pm l)$. Reflections at $(\pm h/2\ k\ l)$ are associated with an anti-parallel shift of Sr cations.

$Sr_3Ca_{1+x}Nb_{2-x}O_{9-\delta}$ also exhibited ordered and disordered domains separated by anti-phase boundaries, as shown in Fig. 4d. Nowick and Du[2] have shown that ordered and disordered domains can coexist in HTPC complex perovskites.The $(\pm 1/2 \pm 1/2 \pm 1/2)$ reflections from $Sr_3Ca_{1+x}Nb_{2-x}O_{9-\delta}$ are stronger than $SrCe_{1-x}Y_xO_{3-\delta}$. Dark field imaging from (1/2 1/2 1/2) revealed bright and dark domains separated by curved anti-phase boundaries (APBs). The bright domains exhibit an ordered

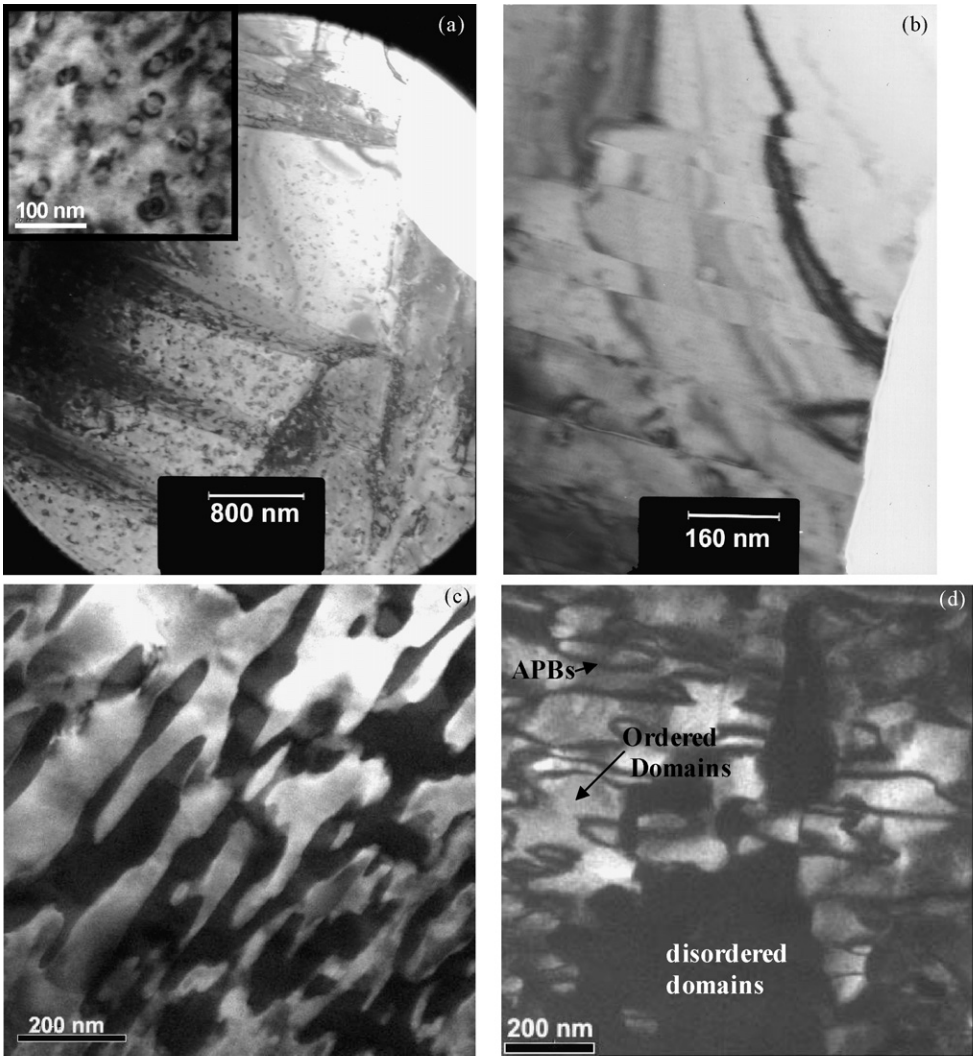

Fig. 4. TEM micrographs showing (a) vacancies loops in $SrCe_{1-x}Y_xO_{3-\delta}$, (b) domains of orientation variants in $SrCe_{1-x}Y_xO_{3-\delta}$, (c) domains of anti-parallel shifts of Sr in $Sr_3Ca_{1+x}Nb_{2-x}O_{9-\delta}$ and (d) domains of 1:1 ordering separated by antiphase boundaries in $Sr_3Ca_{1+x}Nb_{2-x}O_{9-\delta}$.

distribution of B^{2+} and B^{5+} cations on the B site along $\{1\,1\,1\}$ planes. The ordering mode produces a doubling of the periodicity in the $\langle 1\,1\,1\rangle$ direction (1:1 ordering mode). The APBs separated translation variants of this 1:1 ordered distribution.[11] Analyses by STEM-EDAX were obtained across disordered and ordered domains. The Nb^{5+} cation ratio, defined as $Nb^{5+}/(Nb^{5+}+Ca^{2+}+Sr^{2+})$, revealed slight variations from 0.30 to 0.34. These values were associated with local variation of the substitution level from $x=0.18$ (disordered domains) to $x=0$ (ordered 1:1 domains with $B^{5+}/B^{2+}=2$ as described in the random site model). This indicates that the cells in $Sr_3Ca_{1+x}Nb_{2-x}O_{9-\delta}$ were composed of stoichiometric ordered domains surrounded by oxygen deficient disordered domains.

3.3. Microstructure characterization of $BaCe_{0.9}Y_{0.1}O_{3-\delta}$ films

The microstructure of $BaCe_{0.9}Y_{0.1}O_{3-\delta}$ films deposited on porous Al_2O_3 and $BaZrO_3$ were examined by SEM and TEM. PLD produced films with a columnar microstructure on both porous substrates with column widths on the order of 0.2–0.3 μm, as shown Fig. 5. The results demonstrate that dense crystalline protonic films can be deposited onto porous substrates at temperatures as low as 400 °C. In general, dense films have been fabricated over a wide temperature range of 400–950 °C at pressures up to 200 mTorr. No embedded $BaCe_{0.9}Y_{0.1}O_{3-\delta}$ particles are observed in the film microstructure. (Intrinsic “splashing” associated with laser ablation can produce droplets or particles in the plasma plume.) As expected, matching crystal symmetry between substrate and film produced films with lowest defects, e.g., $BaZrO_3$. In comparison to directionally solidified microstructures, no domain structures were observed in the thin film microstructures.

X-ray diffraction (XRD) of deposited films revealed oriented film growth with preferential growth along the [1 0 0] and [0 0 1] direction. Growth of [0 0 1] orientated films appears to be less sensitive to process conditions and predominates under most growth conditions. Growth of the [1 0 0] orientation was observed under low laser pulse energy density. Temperature,

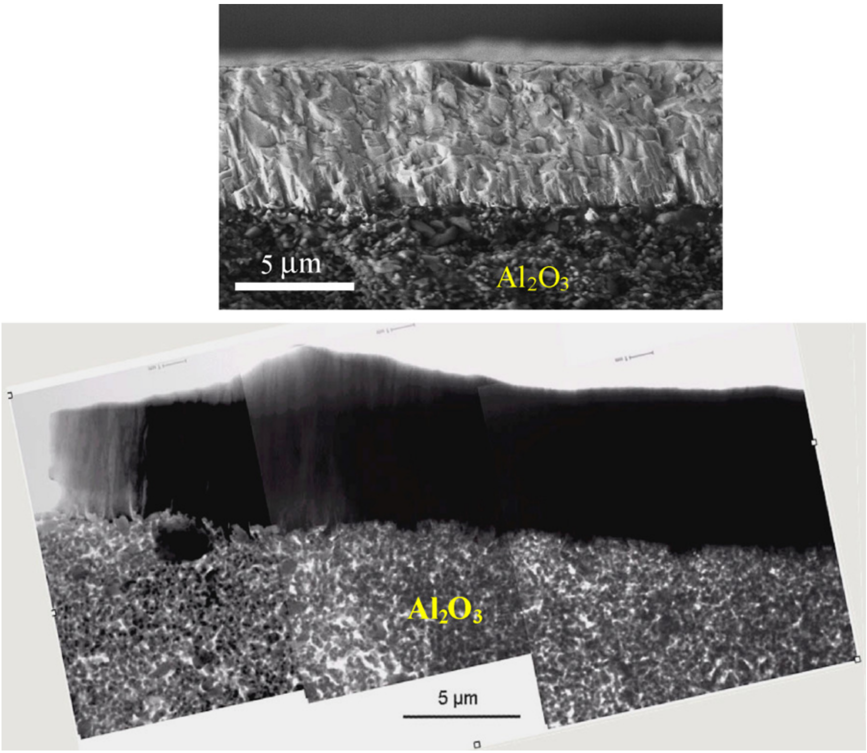

Fig. 5. TEM micrograph of $BaCe_{0.9}Y_{0.1}O_{3-\delta}$ deposited on porous Al_2O_3.

pressure and pulse energy are the main parameters that change film growth. Changing the laser pulse energy changes the kinetic energy of the plume, degree of ionization and amount of ablated material in the vapor.[12,13] Pressure can reduce the kinetic energy of the plume and molecular clusters in the vapor. Film growth under energetic fluxes is well documented in the literature.[14] Oriented film growth dependence upon pressure has been reported in the literature for $BaTiO_3$ films fabricated by PLD.[15] Further work is needed to establish film growth dependency on PLD process conditions.

Fig. 6 shows TEM cross-sections of the $BaCe_{0.9}Y_{0.1}O_{3-\delta}$ films grown on porous Al_2O_3 and $BaZrO_3$ substrates at 800 and 600 °C, respectively. Direct film growth and indirect film growth has been observed on the substrate particles. A distinct interface between the $BaCe_{0.9}Y_{0.1}O_{3-\delta}$ film and porous Al_2O_3 substrate is observed. The Al_2O_3 particles are nucleation sites for $BaCe_{0.9}Y_{0.1}O_{3-\delta}$ film growth. Film growth does not penetrate into the porous Al_2O_3 architecture. HRTEM reveals a thin amorphous $BaCe_{0.9}Y_{0.1}O_{3-\delta}$ layer forms on the Al_2O_3 particles. Nano-cystals of $BaCe_{0.9}Y_{0.1}O_{3-\delta}$ nucleate and grow from the amorphous layer. As the film grows, dominant crystal growth perseveres to form either a [1 0 0] or [0 0 1] orientated film. As the film continues to grow, a dense $BaCe_{0.9}Y_{0.1}O_{3-\delta}$ film is formed by impingement of growing $BaCe_{0.9}Y_{0.1}O_{3-\delta}$ columns. Finally, there appears to be a strong correlation of the film column width with Al_2O_3 particle size. This was an unexpected result but it provides another possible pathway to engineer the film microstructure. Further work is needed to establish the physical size range of this relationship. Our work has shown that a continuous BCY film cannot be achieved on porous substrates with an average pore size of 10 µm.

Non-epitaxial growth is observed on $BaZrO_3$ particles. Two different microstructures have been observed on the porous $BaZrO_3$ substrates. First observation is the formation of an intermediate porous layer of $BaCe_{0.9}Y_{0.1}O_{3-\delta}$ nano-particles between substrate and film. The nano-particles nucleate on the $BaZrO_3$ particles with a size on the order of 100 nm. Fig. 6B shows the region $BaCe_{0.9}Y_{0.1}O_{3-\delta}$ nano-particles; particle composition was confirmed by STEM-EDAX analysis. Growth of [1 0 0] oriented $BaCe_{0.9}Y_{0.1}O_{3-\delta}$ columns originate from the $BaCe_{0.9}Y_{0.1}O_{3-\delta}$ nano-particles. Dense film is formed by growth impingement of the growing columns. The column widths are 0.2–0.8 µm. There appears to be no correlation between $BaZrO_3$ particle size and film column width.

The second observation is the formation of a segregated microstructure on $BaZrO_3$ substrates under identical deposition conditions. Process parameters that caused segregation have not been isolated. Segregated microstructures have been observed at high and low temperature depositions. It should be noted that CeO_2 segregation has been observed for magnetron sputtered $BaCe_{0.9}Y_{0.1}O_{3-\delta}$ films as reported by He et al.[16] Fig. 7A shows a segregated film microstructure. A layer or band microstructure is observed containing layers of nano-crystalline material separated by pseudo-amorphous material. HRTEM shows that the pseudo-amorphous layers contain domains on the order of 2–5 nm. STEM-EDAX analyses shows that the pseudo-amorphous layers are deficient in Ba and the nano-crystalline layers are Ce deficient. Fig. 7B shows that the pseudo-layer nucleated directly on the $BaZrO_3$ particle. Results clearly indicate that further work is required to understand the nucleated growth of $BaCe_{0.9}Y_{0.1}O_{3-\delta}$ films on $BaZrO_3$ particles.

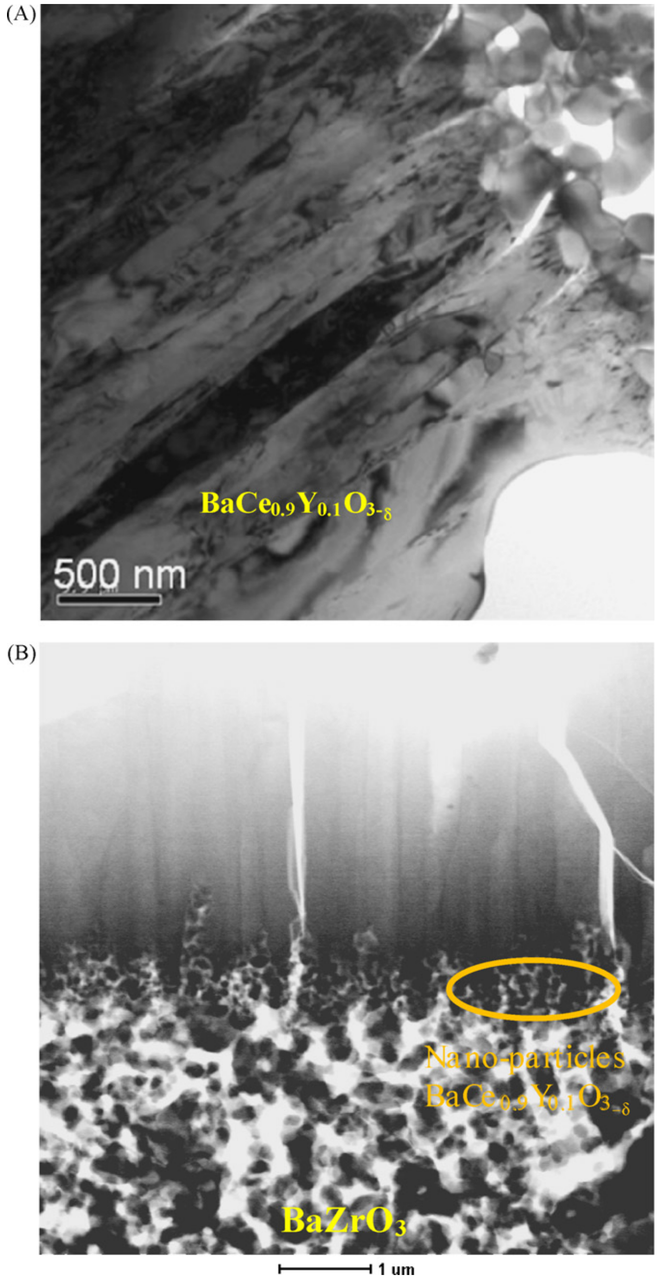

Fig. 6. TEM micrographs of $BaCe_{0.9}Y_{0.1}O_{3-\delta}$ deposited on (A) porous Al_2O_3 and (B) porous $BaZrO_3$.

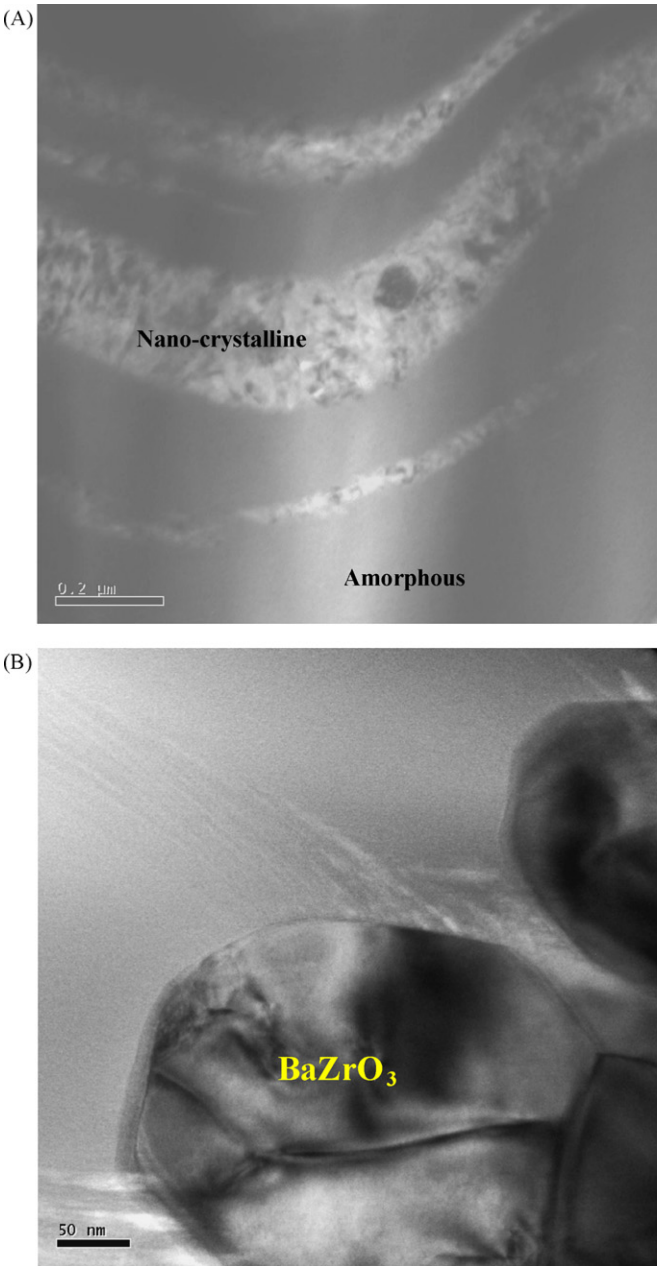

Fig. 7. (A) Amorphous and nano-crytaliine $BaCe_{0.9}Y_{0.1}O_{3-\delta}$ bands. (B) Amorphous $BaCe_{0.9}Y_{0.1}O_{3-\delta}$ growth on $BaZrO_3$.

3.4. *Electrical characterization by electrical impedance spectroscopy*

The electrical properties of $SrCe_{0.9}Y_{0.1}O_{3-\delta}$, $Sr_3Ca_{1+x}Nb_{2-x}O_{9-\delta}$ and $BaCe_{0.9}Y_{0.1}O_{3-\delta}$ films were measured by EIS. The impedance data was analyzed by fitting the spectrums using equivalent electrical circuits: (1) $SrCe_{0.9}Y_{0.1}O_{3-\delta}$: $(RQ)_{Grain} + (R_1Q_1)_{GrainBoundary} + (R_2Q_2)_{GrainBoundary} + (C)_{electrode}$, (2) $Sr_3Ca_{1+x}Nb_{2-x}O_{9-\delta}$: $(RQ)_{Grain} + (RQ)_{GrainBoundary} + (C)_{electrode}$ and (3) $BaCe_{0.9}Y_{0.1}O_{3-\delta}$: $(RQ)_{Grain} + (RQ)_{GrainBoundary} + (E)_{electrode}$, where R = resistance, Q = constant phase element and C = capacitor. A second equivalent circuit was added for the grain boundary in $SrCe_{0.9}Y_{0.1}O_{3-\delta}$ to compensate for the aluminium contamination. The total conductivities were calculated from the impedance data. Circuit parameters for the equivalent circuits were obtained by using the least squares fitting routine in Zview (Scribner Associates) or ZSimpWin (Princeton Applied Research).

The apparent energies for electrical conduction, Q, were determined by plotting σT vs. $1/RT$ using the Arrhenius equation of $\sigma T = A \exp(-Q/RT)$. Fig. 8 shows the Arrhenius plot of the electrical conduction data for $SrCe_{0.9}Y_{0.1}O_{3-\delta}$ and $Sr_3Ca_{1+x}Nb_{2-x}O_{9-\delta}$. The measured total conductivity for directionally solidified $SrCe_{0.9}Y_{0.1}O_{3-\delta}$ is compared to sintered

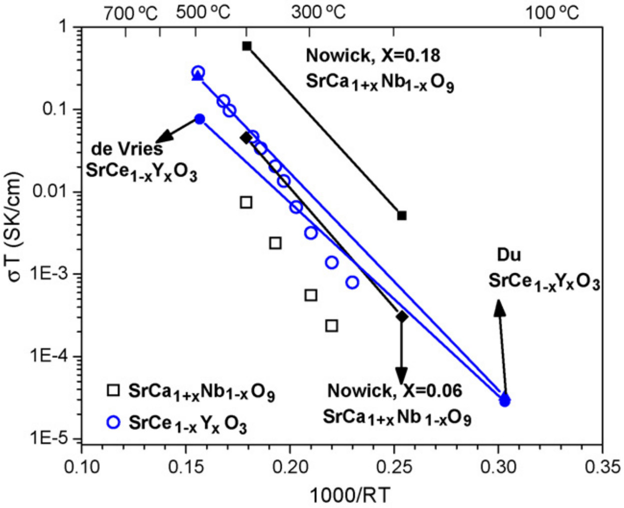

Fig. 8. Total electrical conductivity of melt processed of $SrCe_{0.9}Y_{0.1}O_{3-\delta}$ and $Sr_3Ca_{1+x}Nb_{2-x}O_{9-\delta}$.

$SrCe_{0.95}Yb_{0.05}O_{3-\delta}$ reported by de Vries,[17] Nowick and Du,[2] and Kosacki and Tuller.[18] An activation energy of 83.2 kJ/mol was calculated from the data, higher than report values of 53.6 and 60.8 kJ/mol by de Vries and Nowick and Du, but similar to 77.2 kJ/mol reported by Kosacki and Tuller.

The measured total conductivity for directionally solidified $Sr_3Ca_{1+x}Nb_{2-x}O_{9-\delta}$ is compared to sintered $Sr_3Ca_{1.18}Nb_{1.82}O_{9-\delta}$ and $Sr_3Ca_{1.06}Nb_{1.94}O_{9-\delta}$ reported by Nowick and Du.[2] Conduction is significantly less than Nowick and Du data. Measured activation energy of 84.5 kJ/mol is higher than activation energy reported of 63.6 and 66.5 kJ/mol for $X = 0.18$ and 0.06, respectively. This discrepancy can be explained by microstructural and chemical observations. The actual calcium to niobium ratio was lower than initial composition, solidified sample Ca/Nb ratio was $x \sim 0.1$ instead of $x = 0.18$. It is known from Nowick and Du work that the electrical conductivity of $SrCa_{1+x}Nb_{2-x}O_{9-\delta}$ decreases with decreasing Ca/Nb ratios. The reduction in conductivity occurs because the oxygen non-stoichiometry is dependent on the ratio of bivalent to pentavalent cations (B'^{2+}/B''^{5+}) on the B-site of the perovskite. The cellular $SrCa_{1+x}Nb_{2-x}O_{9-\delta}$ microstructure is unfavorable for protonic transport. The spatial deviation of Ca/Nb ratio from its nominal value is balanced by a decrease in the concentration of the oxygen vacancies from the center to the cell boundary. As a consequence, the boundary can act as resistive barriers for protonic conduction. At the nano-scale, local variations in B'^{2+}/B''^{5+} with respect to the nominal composition induce local variations in the conduction behavior. The microstructure shows the existence of ordered and disordered domains. The ordered domains do not have the mean composition of the rod. They must coexist with disordered domains to balance the global stoichiometry and charge neutrality. Stoichiometric ordered domains are surrounded by oxygen deficient disordered domains.[19] It is clear that the global protonic transport is affected by these nano-scale structures. Further work is required to understand protonic conduction in materials at the nano-scale.

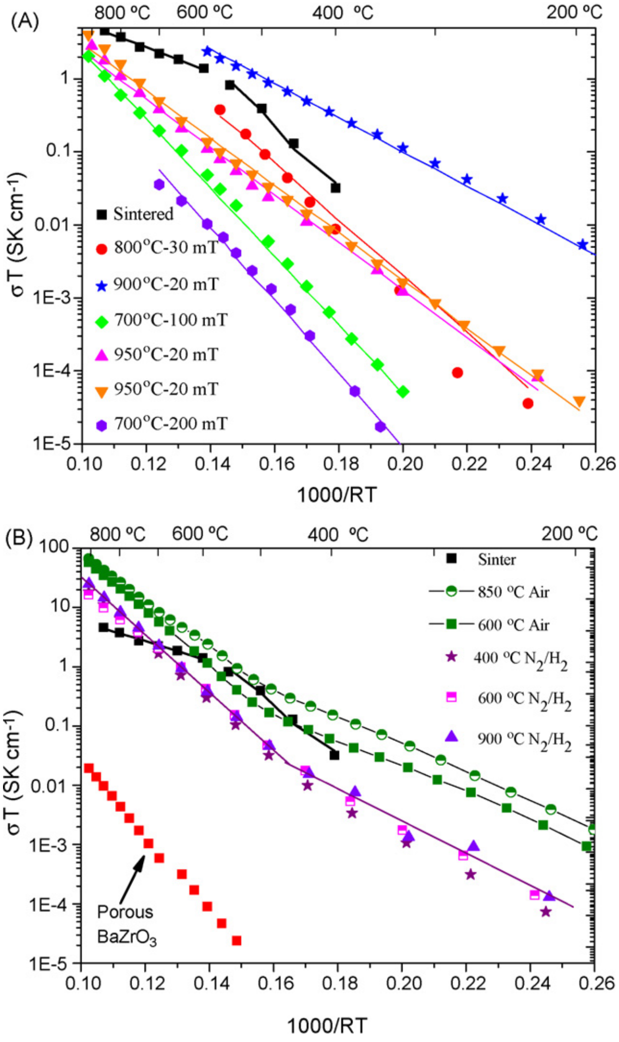

Fig. 9. Total electrical conductivity of $BaCe_{0.9}Y_{0.1}O_{3-\delta}$ film on (A) porous Al_2O_3 and (B) porous $BaZrO_3$.

Fig. 9 shows the Arrhenius plot of the electrical conductivity of $BaCe_{0.9}Y_{0.1}O_{3-\delta}$ films deposited on porous Al_2O_3 and $BaZrO_3$. It should be noted that electrical conduction of the film was measured perpendicular to the film growth direction. A sintered $BaCe_{0.9}Y_{0.1}O_{3-\delta}$ specimen was used as a reference sample. Fig. 9 shows that the film electrical conductivity is highly dependent on process parameters for Al_2O_3 but nearly independent of process parameters when deposited on $BaZrO_3$. $BaCe_{0.9}Y_{0.1}O_{3-\delta}$ films deposited on $BaZrO_3$ exhibit superior electrical conduction than sintered $BaCe_{0.9}Y_{0.1}O_{3-\delta}$ above 550 °C. Film thickness dependence has been reported in the literature for oxide films with thicknesses below 1 μm.[20] The results show no evidence of electrical conduction dependence upon film thickness.

Electrical conductivity of $BaCe_{0.9}Y_{0.1}O_{3-\delta}$ films on Al_2O_3 shows dependence on deposition temperature and pressure. A large variation in conductivity is observed. The activation energies ranged from 54.1 to 115.6 kJ/mol. Published activation energies for $BaCeO_3$ compositions ranged from 30 to 100 kJ/mol.[21,22] The crystal symmetry mismatch between

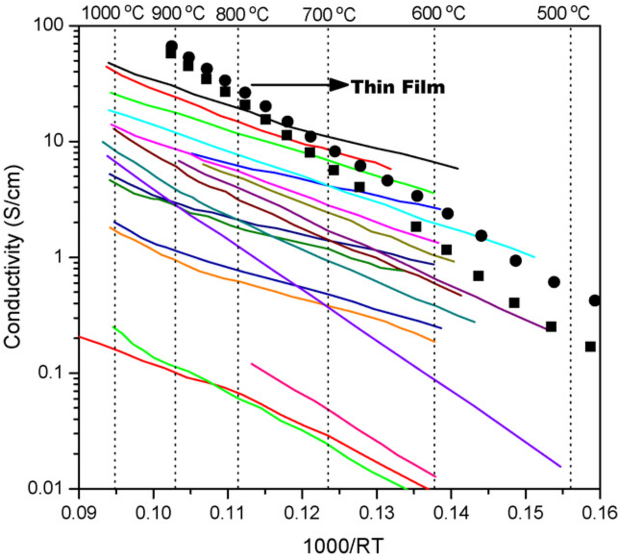

Fig. 10. Comparsion of electrical conductivity of $BaCe_{0.9}Y_{0.1}O_3$ films to published data on protonic ceramics[23]; compositions listed start from top to bottom: $BaCe_{0.95}Y_{0.05}O_3$, $BaCe_{0.9}Nd_{0.1}O_3$, $BaCe_{0.5}Zr_{0.4}Y_{0.1}O_3$, $BaCe_{0.95}Gd_{0.05}O_3$, $SrCe_{0.95}Tm_{0.05}O_3$, $BaZr_{0.95}Rh_{0.05}O_3$, $SrCe_{0.95}Yb_{0.05}O_3$, $SrZr_{0.95}Yb_{0.05}O_3$, $SrCe_{0.95}Ho_{0.05}O_3$, $SrCe_{0.95}Y_{0.05}O_3$, $SrZr_{0.95}Y_{0.05}O_3$, $SrCe_{0.95}Sc_{0.05}O_3$, $SrCe_{0.95}Rh_{0.025}Y_{0.025}O_3$, $SrZr_{0.95}In_{0.05}O_3$, $SrCe_{0.95}Eu_{0.05}O_3$, $SrZr_{0.95}Al_{0.05}O_3$, $SrZr_{0.95}Ga_{0.05}O_3$ and $SrZrO_3$.

$BaCe_{0.9}Y_{0.1}O_{3-\delta}$ and Al_2O_3 suggest that strain may restrict proton transport.

Matching crystal symmetry between film and substrate significantly reduced electrical conductivity dependence upon deposition parameters. Fig. 9 shows that $BaZrO_3$ is highly resistive to conduction compared to the film; leakage by the substrate is negligible. The data show different activation energies at high and low temperatures. Activation energies of 89.7–112.2 kJ/mol was observed at high temperatures, whereas values of 45.7–62.5 kJ/mol was observed at low temperatures. The high temperature activation energies are higher than normally observed for most HTPC materials[23] as shown in Fig. 10. High temperature dependent electrical conduction behavior matches well with $SrCe_{0.95}Eu_{0.05}O_3$ and $SrZr_{0.95}Al_{0.05}O_3$. The change in conduction behavior at low and high temperatures is not known. It is also interesting that the conduction behavior of the cation segregated films mimic the non-segregated film as shown in Fig. 9. It should be noted that the segregated films were measured in a gas environment of 5% H_2/95% N_2 instead of air. It is clear that the information derived from the conductivity experiments is not sufficient to identify the mechanistic features of proton transport. Understanding proton transport in solids remains a challenge.

4. Conclusions

Low temperature fabrication of dense $BaCe_{0.9}Y_{0.1}O_{3-\delta}$ films was achieved on porous Al_2O_3 and $BaZrO_3$ substrates by PLD. Dense films occur by impingement of the growing columnar grains. Electrical impedance spectroscopy revealed high conducting $BaCe_{0.9}Y_{0.1}O_{3-\delta}$ films when deposited on $BaZrO_3$. Crystal symmetry between substrate and film is important; non-epitaxial growth was not observed for films deposited on $BaZrO_3$. Two activation energies for conduction were observed for $BaCe_{0.9}Y_{0.1}O_{3-\delta}$ films deposited on $BaZrO_3$; data exhibit slopes of 89.7/112.2 and 45.7/62.5 kJ/mol at temperatures above 550 °C and below 550 °C. The data were insufficient to elucidate the mechanism for change in the temperature dependent conduction behavior.

Unique microstructures of $SrCe_{1-x}Y_xO_{3-\delta}$ and $Sr_3Ca_{1+x}Nb_{2-x}O_{9-\delta}$ ceramics were achieved by directional solidification. Textured microstructure of $SrCe_{1-x}Y_xO_{3-\delta}$ contained an undesirable aluminium rich intra-granular phases. The second phases were enriched in hydrogen but were highly resistant to proton transport suggesting a mechanism of proton trapping. The cellular microstructure of $Sr_3Ca_{1+x}Nb_{2-x}O_{9-\delta}$ was found to be unfavorable for protonic transport due to the chemical gradient of the Ca/Nb ratio from the cell center to the cell boundary. This work has revealed a high density of defects in the perovskite materials such as boundaries between orientation variants, ordered/disordered domains, anti-phase boundaries and vacancy loops. The resistivity of the melt-processed samples was similar to published values for sintered samples. Further work is needed to understand the impact of these defects on the global proton transport.

Acknowledgments

Financial support for this work was obtained from following sources: (1) NASA Glenn Research Center, Brookpark, Ohio under cooperative agreement NCC3-850 through NASA's Internal Research and Development Program and (2) European Office of Aerospace Research and Development funded by AFOSR under grant no. FA8655-03-1-3040.

References

1. Iwahar, H. *et al.*, *Solid State Ionics*, 1983, **11**, 109.
2. Nowick and Du, *Solid State Ionics*, 1995, **77**, 137.
3. Nowick *et al.*, *Solid State Ionics*, 1999, **125**, 303.
4. Lopez-Robledo *et al.*, *Solid State Ionics*, 2007, **178**, 207.
5. Berger *et al.*, Solid State Ionics. *177*, 2006, 2339.
6. Dynys *et al.*, *Solid State Ionics*, 2006, **177**, 2333.
7. Dynys *et al.*, *Ceram. Eng. Sci. Proc.*, 2004, **25**, 293.
8. Berger, *Solid State Ionics*, 2006, **177**, 1655.
9. Reaney *et al.*, *Jpn. J. Appl. Phys.*, 1994, **33**, 3984.
10. Colla *et al.*, *J. Appl. Phys.*, 1993, **74**, 3414.
11. Davies, *Curr. Opin. Solid State Mater. Sci.*, 1999, **4**, 467.
12. Tasaka *et al.*, *Thin Solid Films*, 1996, **281–282**, 441.
13. Kreutz and Gottmann, *Phys. Status Solidi (A)*, 1998, **166**, 569.
14. Chrisey, ed., *Pulsed Laser Deposition of Thin Films*. Wiley & Sons, NY, 1994.
15. Kim *et al.*, *Mater. Lett.*, 1999, **40**, 146.
16. He *et al.*, *Solid State Ionics*, 1996, **89**, 9.
17. de Vries, *Solid State Ionics*, 1997, **100**, 173.
18. Kosacki and Tuller, *Solid State Ionics*, 1995, **80**, 175.
19. Reichel *et al.*, *Solid State Ionics*, 1996, **86–88**, 639.
20. Kosacki *et al.*, *Solid State Ionics*, 2005, **176**, 1319.
21. Coors and Readey, *J. Am. Ceram. Soc.*, 2002, **85**, 2637.
22. Meng *et al.*, *Solid State Ionics*, 2000, **136–137**, 209.
23. Gupta and Lin, *Dense Ceramic Membranes*, *49*, ed. Sammauls and Mundschau. Wiley-VCH, 2006.